Journal of Southeast University (English Edition) Vol. 40, No. 4, pp. 363 – 371 Dec. 2024 ISSN 1003—7985

Influence of inflow conditions on the hydrodynamic characteristics of floating photovoltaic membrane structures

Zhang Puyang Zhang Linyang Xiong Lichao Le Conghuan Ding Hongyan

(State Key Laboratory of Hydraulic Engineering Intelligent Construction and Operation, Tianjin University, Tianjin 300072, China)

Abstract: The floating photovoltaic membrane prototype developed by Ocean Sun was selected as a reference object, and a 1∶40 scale laboratory model was designed and produced to further explore the impact of inflow conditions on the hydrodynamic properties of the membrane structure. By conducting free attenuation tests, results showed that the inflow has only a slight effect on the natural frequencies of the heave, pitch, and surge of the membrane structure. This finding shows that the dynamic properties of the membrane structure remain essentially stable under different inflow conditions. The results of further regular and irregular wave hydrodynamic experiments show that, compared with the control group, the response of the membrane structure under inflow conditions in terms of heave, pitch, surge, and heave acceleration motions is relatively gentle, whereas the response of the membrane structure to the mooring force is strong. Especially when the waves are irregular, the inflow conditions have a more significant impact on the membrane structure, which may lead to more complex response changes in the structure. Therefore, in the actual engineering design process, the impact of inflow conditions on the behavior of the membrane structure must be fully considered, and appropriate engineering measures must be taken to ensure the safety and stability of the structure.

Key words: floating photovoltaic; membrane; hydrodynamic characteristic; inflow

DOI: 10.3969/j.issn.1003 – 7985.2024.04.005

As China promises to peak carbon dioxide emissions in 2030 and strives to achieve carbon neutrality by 2060, effectively controlling carbon emissions from building structures has become a new trend in green development[1]. Because of the increasingly serious global environmental problems and the increasing demand for and awareness of renewable energy, photovoltaic power generation has become one of the fastest-growing clean energy sources[2]. Among them, floating photovoltaic (FPV) systems have emerged as a promising frontier in the realm of renewable energy[3-4].

A large number of countries have enacted policies aimed at incentivizing and supporting the development of FPV systems[5]. Moreover, as technology continues to mature and costs gradually decrease, there has been a global surge in large-scale investments in FPV construction[6]. Several notable high-capacity FPV projects in recent years include the 60 MWp FPV installed at the Western Reservoir in Singapore[7]; 41 MWp FPV at the Hapcheon Dam in South Korea[8]; 320 MWp FPV project at the Dezhou Reservoir in Shandong, China[9]; 45 MWp FPV at the Sirindhorn Dam in Thailand[9]; 13.7 MWp FPV at the Yamakura Dam in Japan[10]; 4.8 MWp FPV at the Healdsburg Wastewater Treatment Plant in California, USA[11]; 41.1 MWp FPV in Groningen, the Netherlands[12]; 5 MWp FPV at the Alqueva Hydroelectric Power Station in Portugal[13]; and 0.5 MWp FPV at the South No. 3 Offshore Wind Farm on the Shandong Peninsula in China[14]. The implementation of these FPV projects will not only expand the construction experience but also drive technological development[15].

Within the realm of FPV projects, the application of membrane structures as novel floating structures is garnering increasing attention. The membrane design boasts exceptional hydrodynamic stability, superior economic performance, and heightened power generation efficiency because of the cooling effect. Kjeldstad et al.[16] analyzed the performance and quantified the cooling effect of the FPV membrane technology and determined that the membrane resting on the water body exhibits a 5%-7% higher yield on average than that cooled by air. An example of this innovative approach is evident in the collaboration between Ocean Sun and Statkraft, marked by an agreement to construct four PV floaters at the Banja Hydropower Plant in Albania[17]. This pioneering venture highlights the efficiency and viability of membrane structures in the challenging and dynamic environment of water-based solar installations and is poised to exemplify the potential of membrane technology in the FPV landscape.

Despite the growing prominence of membrane structures for their flexibility, cost-effectiveness, and adaptability to varying water environments, they are not without flaws. Among these, encountering high waves is considered one of the most serious challenges in the marine en-

Received 2024-05-01, **Revised** 2024-09-10.

Biography: Zhang Puyang (1978—), male, doctor, associate professor, zpy_td@163.com.

Foundation item: The National Natural Science Foundation of China (No. 52171274).

Citation: Zhang Puyang, Zhang Linyang, Xiong Lichao, et al. Influence of inflow conditions on the hydrodynamic characteristics of floating photovoltaic membrane structures[J]. Journal of Southeast University (English Edition), 2024, 40(4): 363 – 371. DOI: 10.3969/j.issn.1003 – 7985.2024.04.005.

vironment as it can lead to structural inundation (inflow), which may result in the failure of structural components, thereby diminishing power generation efficiency. In addition, it could impact the hydrodynamic performance of the structure, posing potential risks. Therefore, considering the occurrence of inflow, an unconventional condition is crucial for maintaining the safe operation of the structure.

This academic endeavor aims to unravel the hydrodynamic intricacies inherent in FPV membrane structures under inflow conditions. By delving into the dynamics of water body interactions and the impact of inflow on floating membrane structures, we seek to contribute valuable insights into the growing body of knowledge in renewable energy research.

1 Experimental Methodology

1.1 Laboratory-scale model

Referring to the prototype structure of Ocean Sun, a 1∶40 scale model was designed and fabricated for the laboratory tests (see Fig. 1). After the calculations, the characteristic diameter of the model is 1.25 m, and the total mass is 4.9 kg. The model mainly consists of three parts: floating rings, membranes, and fasteners. In addition, connecting ropes are used to link the floating rings and membrane. The buoyancy of the structure is provided jointly by the floating rings and membrane[18].

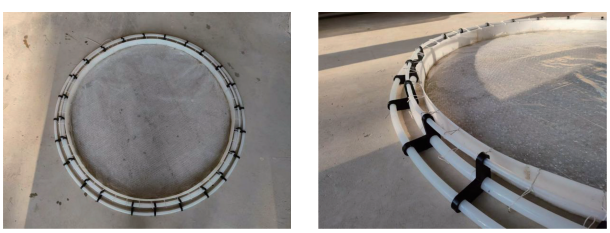

(a) (b)

Fig. 1 Laboratory-scale model. (a) Model top view; (b) Model border details

The membrane is composed of two parts, namely, horizontal multilayer films and disk-shaped ring films. The horizontal multilayer film has a diameter of 1.1 m and a thickness of 2 mm and comprises at least three layers. This study simplifies it into upper-layer polyethylene (PE) material film, middle-layer foam bubble film, and lower-layer PE material film to ensure structural flexibility. The disk-shaped ring film is similar to a disk-shaped PE film with a slightly inclined side. The bottom diameter is 1.10 m, and the top diameter is 1.15 m. The disk-shaped ring film has a certain degree of hardness to maintain the shape of the structure. An industrial adhesive is used to connect the horizontal multilayer film and the disk-shaped ring film to ensure that the structure is waterproof.

The floating ring consists of three structures, namely, inner, outer, and top rings. Table 1 lists the relevant dimensional parameters of the floating rings. The center of the bottom membrane and the bottom floating ring are set at the same height, designated as 0. The outer ring is the outermost ring with the largest diameter, responsible for bearing the primary wave loads. The inner ring is located below the inner circle and, together with the outer ring, provides buoyancy for the structure. The top ring is the uppermost ring in the inner circle. These rings are all connected to the membrane via the connecting ropes.

Table 1 Dimensional parameters of the floating ring

Floating ring	Cross-sectional diameter/mm	Cross-sectional thickness/mm	Height/cm	Diameter/m	Length/m
Inner ring	20	2	0	1.2	3.77
Outer ring	16	2	0	1.3	4.10
Top ring	10	2	5	1.2	3.77

The fasteners are made of 3D-printed PE plastic and are utilized to fix the three floating rings. The scaled model uses only 24 fasteners for connection, ensuring structural stability and integrity while meeting the similarity criterion. Table 2 provides the material parameters for each component. Specifically, the horizontal film is made of high-density PE, and the ring-shaped film is made of low-density PE.

Table 2 Material parameters of the components

Components	Density/(g·cm^{-3})	Thickness/mm	Young's modulus/GPa	Shear modulus/GPa	Poisson's ratio
Floating ring	1.1	2	0.36	0.24	0.25
Fastener	2.3	10	1.07	0.37	0.41
Disk-shaped film	0.7	1.5	0.13	0.05	0.38
Horizontal film	0.5	2			

The mooring system employs four anchor points located at the front, rear, left, and right of the model. Each anchor point is connected to the edge of the structure by an anchor chain in a catenary state. The specifications of the mooring chain are a length of 2.1 m, a diameter of 2 mm, a mass of 0.04 kg, and a minimum breaking force of 2.25 kN.

1.2 Test introduction

The tests in this study were conducted at the State Key Laboratory of Hydraulic Engineering Simulation and Safety at Tianjin University (see Fig. 2). The site consists of a water tank, wave generator, model, wave absorbers, brackets, equipment, and instruments. In the test, seven wave generators were arranged side by side to meet the wave generation requirements. The model was positioned in the middle of the wave generators to prevent the interference caused by wave spreading. The wave absorbers were placed on the other side of the water tank to eliminate the interference waves generated by the reflection of

waves hitting the walls. The brackets were used to secure the sensors; their wiring was made from thin-diameter iron rods to avoid interference with the experiment. The monitoring station was located on the shore next to the water tank to observe the experimental phenomena and record the data collected by the sensors during the experiment.

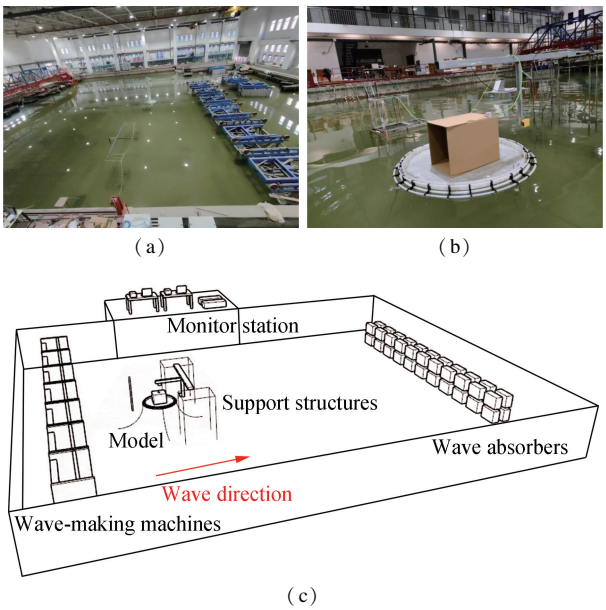

Fig. 2 Laboratory-scale model tests. (a) Laboratory of hydraulic engineering simulation; (b) Scale model test; (c) Layout sketch of the test site

The measurement devices used in the experiment include the high-precision aviation gyroscope, three-wire voltage output laser displacement sensors, voltage-based tension load cell, and digital wave height measurement instrument (see Fig. 3). A gyroscope was employed in the experiment, placed horizontally facing the wave generator direction with its positive side. Because of the symmetry of the structure, this study focuses on the pitch and heave acceleration motions of the model. Four tension load cells were used to measure the tension in each of the four mooring cables. Wave height gauges were used to measure the amplitude and period of the waves. The data from these gauges were analyzed, and more reliable data were selected for further study. Upon validation, the collected wave height data can be deemed reliable if it adheres to a normal distribution pattern. Two laser displacement sensors, with a sampling interval of 1 ms, were used to measure the surging and heaving of the model. The data acquisition system used was the signal measurement and control equipment, capable of simultaneously recording data from four load cells and two laser displacement sensors.

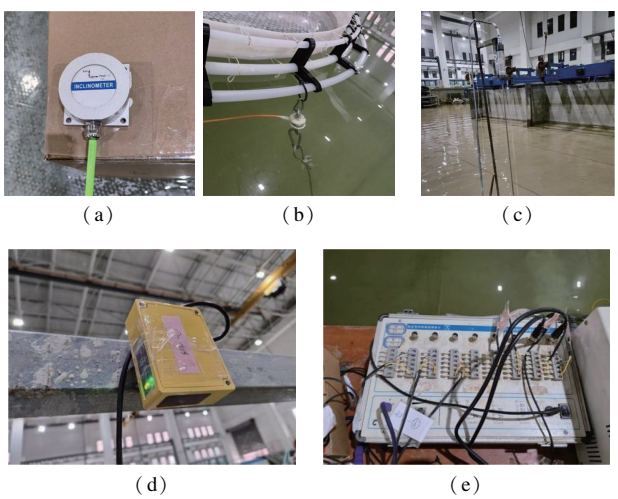

Fig. 3 Measurement instruments employed in the tests. (a) Gyroscope; (b) Tension load cell; (c) Wave height gauge; (d) Laser displacement sensor; (e) Data acquisition system

2 Free Damping Tests

2.1 Experimental procedures

In this study, free decay tests for heaving, surging, and pitching of the floating membrane structure were conducted in still water, and time-history curves were plotted. Through the Fourier transform, the curves of structural amplitude and phase changing with wave frequency were obtained, which helps us understand the natural period of the structure and its dynamic response during free vibration.

Free decay tests were conducted separately for the inflow condition and control groups. The mass of the control group structure was the original model mass of 4.9 kg, whereas the inflow condition group added 2.5 kg of water to the model. Before the test, a certain initial displacement was first applied to the structure and then released to allow the structure to undergo periodic oscillatory motion. The data with higher accuracy in the series of test results were selected for subsequent analysis. Because the starting point of the manual control intervention is more complicated, the obtained curve was scaled to ensure the uniformity and consistency of its starting point.

2.2 Results analysis

In the study of the free decay of heaving, a vertical downward initial displacement of 5 cm was applied to the structure, and the vertical displacement motion of the structure was recorded after release. Because of the significant buoyancy of the structure, the decay is rapid; thus, the first 2 s of the decay curve were analyzed.

Fig. 4 shows that, under the vertical downward initial displacement of 5 cm, the structure first rebounds upward to approximately 3 cm beyond the equilibrium position and then rapidly decays. The examination of the amplitude-frequency curve revealed that the sole peak of the curve is around $x = 1$ Hz, indicating the inherent heave period of the structure is approximately 1 s. The phase-frequency curve showed significant differences in phase

response near the natural period of the structure. Overall observations indicate that the free decay curves for the inflow condition and control groups are highly similar. This finding indicates that, with an increase in inflow, minimal variation occurs in the inherent period of heaving.

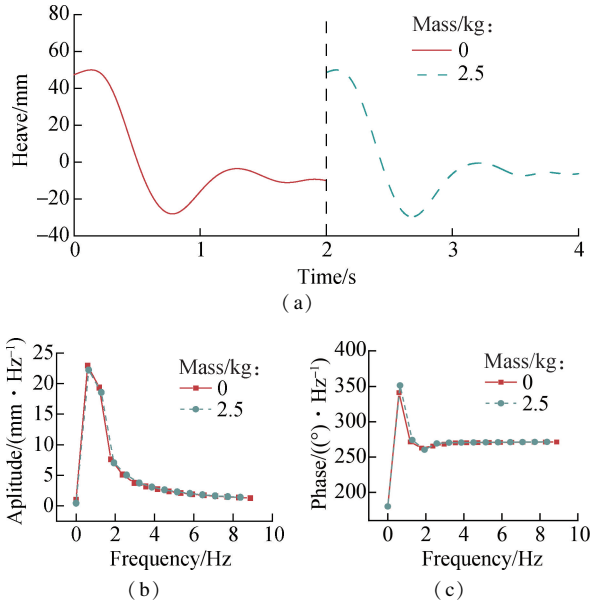

Fig. 4 Free decay test curve of heaving. (a) Time-history curve; (b) Amplitude-frequency curve; (c) Phase-frequency curve

In the study of the free decay of surging, a horizontal initial displacement of 30 cm was applied to the model, and the subsequent horizontal displacement motion of the structure was recorded after release. Because the decay of the surge motion is relatively slow, the first 30 s of the decay curve were chosen for analysis.

Fig. 5 shows that, under the horizontal initial displacement of 30 cm, the structure first rebounds in the opposite direction to approximately 12 cm beyond the equilibrium position and then slowly decays. The examination of the amplitude-frequency curve revealed that the unique peak of the curve is around $x = 0.067$ Hz, indicating that the inherent period of the surge motion is approximately 15 s. The phase-frequency curve showed significant differences in the phase response near the inherent period of the structure. Overall observations indicate that the free decay curves for the inflow condition and control groups are highly similar. This finding indicates that, with an increase in inflow, minimal variation occurs in the inherent period of surging. However, the peak amplitude of surging in the inflow condition group is slightly lower than that in the control group because of the increased damping effect of water on the structure, making the surge motion more prone to decay compared with that of a lightweight structure.

In the study of the free decay of pitching, an initial rotation angle of 10° was applied to the model, and the subsequent rotational motion of the structure was recorded

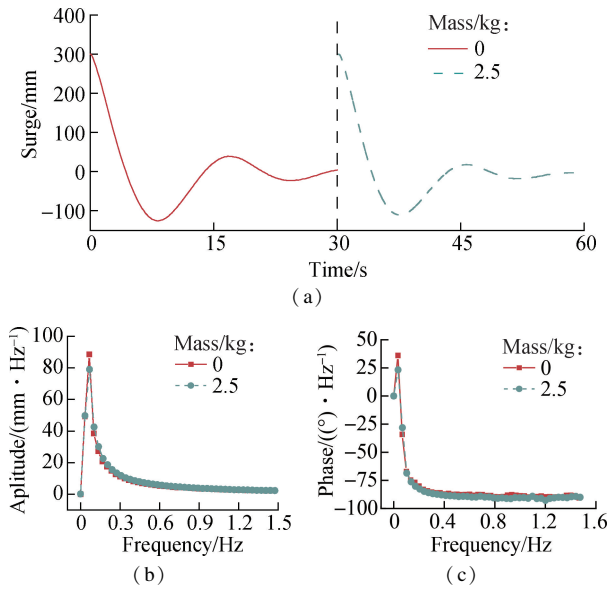

Fig. 5 Free decay test curve of surging. (a) Time-history curve; (b) Amplitude-frequency curve; (c) Phase-frequency curve

after release. Because the structure has significant buoyancy, decay occurs relatively quickly; thus, the first 2.5 s of the decay curve were chosen for analysis.

Fig. 6 shows that, with the 10° rotation, the structure first rebounds in the opposite direction to approximately 9° beyond the equilibrium position and then gradually decays, with the second peak and subsequent decay occurring more rapidly. The amplitude-frequency curve revealed that the unique peak of the curve is around $x = 1.25$ Hz, indicating that the inherent period of the pitch motion is approximately 0.8 s. The phase-frequency curve showed significant differences in the phase response near the inherent period of the structure. Overall observations indicate that the free decay curves for the inflow condition and control groups are highly similar. This

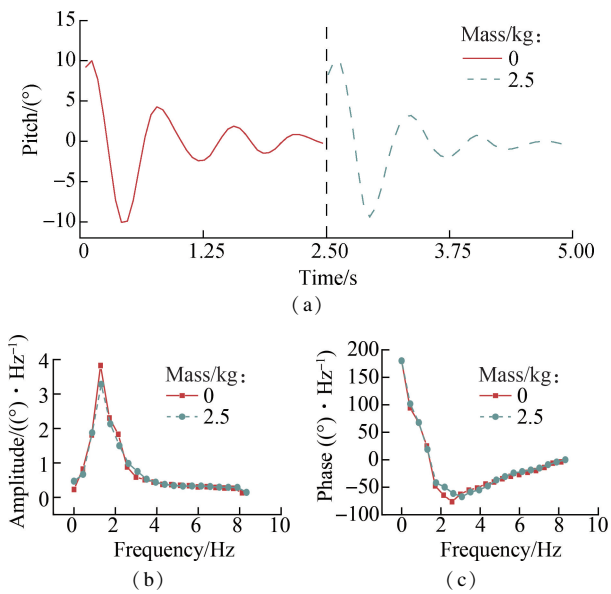

Fig. 6 Free decay test curve of pitching. (a) Time-history curve; (b) Amplitude-frequency curve; (c) Phase-frequency curve

finding indicates that, with an increase in inflow, minimal variation occurs in the inherent period of pitching.

3 Results and Discussion

3.1 Experimental conditions

This section primarily investigates the influence of inflow issues on the time-domain response of the membrane structure, conducting experiments with both regular and irregular waves. The Airy spectrum is used for regular waves, and the JONSWAP spectrum with a spectrum peak factor of 3.3 is used for irregular waves. The duration of each test is 300 s. Among these, 20 s of stable curves under regular wave conditions are selected for analysis, whereas 60 s of valid data under irregular wave conditions are chosen for analysis. The testing conditions are listed in Table 3. The test was conducted using a constant wave with a period of 1.5 s and a significant wave height of 9.5 cm.

Table 3 Testing conditions

Conditions	Wave period/s	Wave height/cm	Model mass/kg	Water depth/m
Inflow condition group	1.5	9.5	7.4	1
Control group	1.5	9.5	4.9	1

3.2 Hydrodynamic analysis under regular wave conditions

As shown in the figures, the time-history curves under regular wave conditions exhibit a well-defined harmonic waveform, indicating the reliability of the data.

Fig. 7 shows that the average peak value of heaving for the control group is 43.9 mm, whereas that for the inflow condition group is 36.3 mm, resulting in a difference of 7.6 mm. This phenomenon indicates that the heave response of the inflow condition group under the specified wave loading is smaller than that of the control group because the membrane structure is classified as a lightweight structure, and the undulations with waves are more pronounced in the absence of inflow. The inflow condition group, with a larger total model mass, is less easily propelled by waves in the vertical direction.

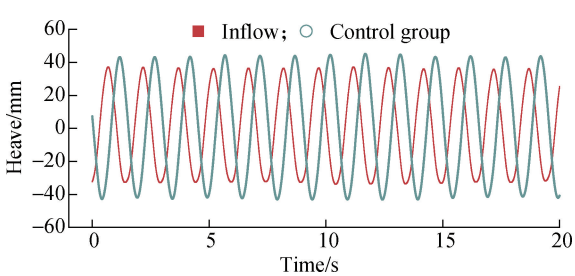

Fig. 7 Time-history curve of heaving

Fig. 8 shows that the average peak value of pitching for the control group is 4.0°, whereas that for the inflow condition group is 3.8°, resulting in a difference of 0.2°. This phenomenon indicates that the pitch response of the inflow condition group under the specified wave loading is slightly smaller than that of the control group, and the increase in model mass has a relatively small impact on the structural pitch motion.

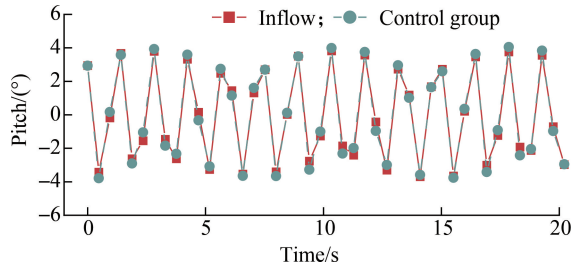

Fig. 8 Time-history curve of pitching

Fig. 9 shows that the curve undergoes reciprocal motion near the 1g gravitational acceleration of Earth. The absolute value of the acceleration generated during the weightless state of the model is greater than the acceleration generated during the overweight state of the model. Therefore, analyzing the acceleration amplitude during the weightless state is more meaningful. The peak amplitude of heave acceleration for the control group is 1.0 m/s^2, whereas that for the inflow condition group is 0.8 m/s^2, resulting in a difference of 0.2 m/s^2. This phenomenon indicates that the heave acceleration of the inflow condition group under the specified wave loading is smaller than that of the control group. This conclusion is consistent with the aforementioned pattern, where the heave response of the inflow condition group is smaller than that of the control group.

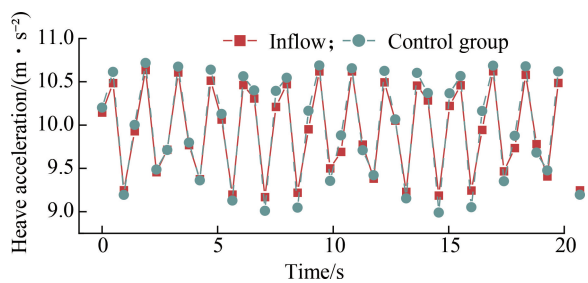

Fig. 9 Time-history curve of heave acceleration

Fig. 10 shows that the average peak value of surging for the control group is 16.2 mm, whereas the average peak value of surging for the inflow condition group is 15.4 mm, resulting in a difference of 0.8 mm. This phenomenon indicates that the surge response of the inflow condition group under the specified wave loading is smaller than that of the control group because of the increase in the total model mass caused by inflow, making the structure less easily propelled by waves. However, the influence of inflow conditions on the structural surge motion is not prominent.

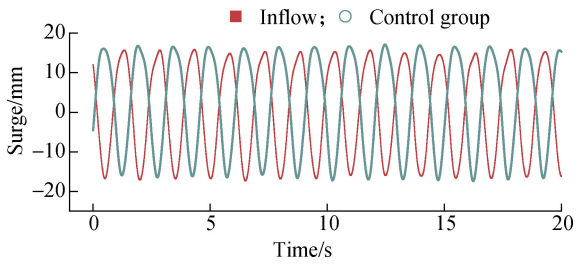

Fig. 10 Time-history curve of surging

The mooring cables have initial stress, and here, the data are analyzed after linear zeroing. Fig. 11 shows that the average peak value of the mooring force of the control group is 0.38 N, whereas that of the inflow condition group is 0.41 N, resulting in a difference of 0.03 N. This phenomenon indicates that the mooring force of the inflow condition group under the specified wave loading is greater than that of the control group because of the increase in the total model mass, which requires a larger mooring force to constrain the motion of the model.

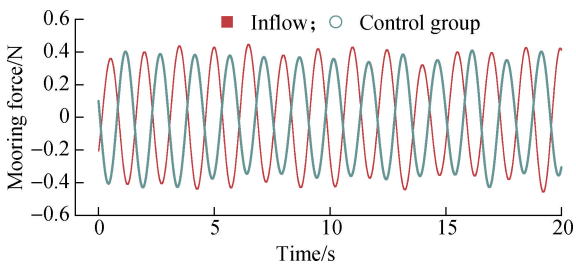

Fig. 11 Time-history curve of mooring force

3.3 Hydrodynamic analysis under irregular wave conditions

The investigation of the motion response of the model under irregular waves is of great importance for the analysis of the structural hydrodynamic characteristics. When assessing the heave, pitch, and surge acceleration responses, waveforms after a certain period of model motion were selected for analysis to avoid insufficient wave action, ensuring that the peak values on the time-history curves approximately follow a normal distribution. When analyzing surge and mooring force, given that the model experiences substantial surge motions deviating from the equilibrium position, the initial 10 s before significant wave action was selected as the start time.

The analysis revealed that the time-history curve under irregular wave conditions is time-ergodic, indicating that the various responses of the model are well-behaved over time. Because of the consistent operational mode of the wave generator, the generated waveforms across all groups exhibit uniform characteristics.

Fig. 12 shows that the power spectral density is concentrated at approximately 0.67 Hz, corresponding to the effective wave period of 1.5 s. The power spectral density in the inflow condition group is lower than that in the control group, indicating that the heave response of the inflow condition group is smaller than that of the control group. Mathematical statistical analysis indicates that the maximum peak values of heave in the inflow condition group are smaller, i.e., an 11% reduction, than that in the control group. The irregular wave situation follows the same pattern as the regular wave discussed previously, further confirming the conclusions.

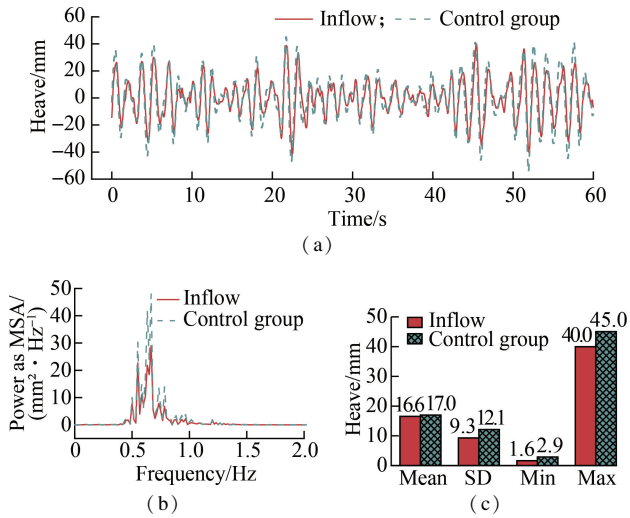

Fig. 12 Analysis of heave motion. (a) Time-history curve; (b) Power spectral density; (c) Mathematical statistics

As shown in Fig. 13, the power spectral density of pitching is relatively scattered, which is attributed to the large sampling interval of the gyroscope, leading to lower data accuracy in the Fourier transform. Mathematical statistical analysis indicates that the various parameters of the pitch in the inflow condition group are smaller than those in the control group, with the maximum peak values exhibiting a decrease of 17%. Under irregular wave conditions, the observed phenomena are consistent with the

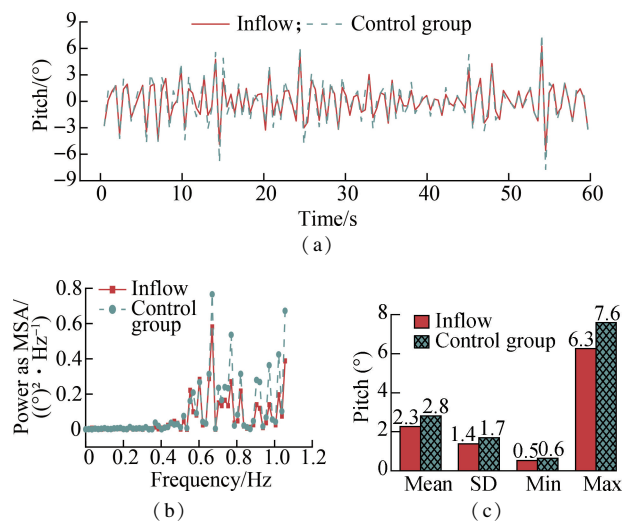

Fig. 13 Analysis of pitch motion. (a) Time-history curve; (b) Power spectral density; (c) Mathematical statistics

overall pattern discussed previously for regular waves but with larger numerical differences. This finding indicates that the increased total mass of the model has a more pronounced inhibitory effect on pitch motion in random waves.

Fig. 14 shows that the heave acceleration curve under irregular wave conditions undergoes reciprocal motion around the 1g gravitational acceleration of Earth. Mathematical statistical analysis indicates that the various parameters of heave acceleration in the inflow condition group are generally smaller than those in the control group, with the maximum peak values exhibiting a reduction of 23%. This finding indicates that inflow conditions have a reducing effect on heave acceleration, consistent with the observed patterns of heave motion discussed previously. The observed patterns under irregular wave conditions are generally consistent with those under regular waves discussed previously but with larger numerical differences. This finding indicates that the increased total mass of the model has a more pronounced reducing effect on heave acceleration in random waves.

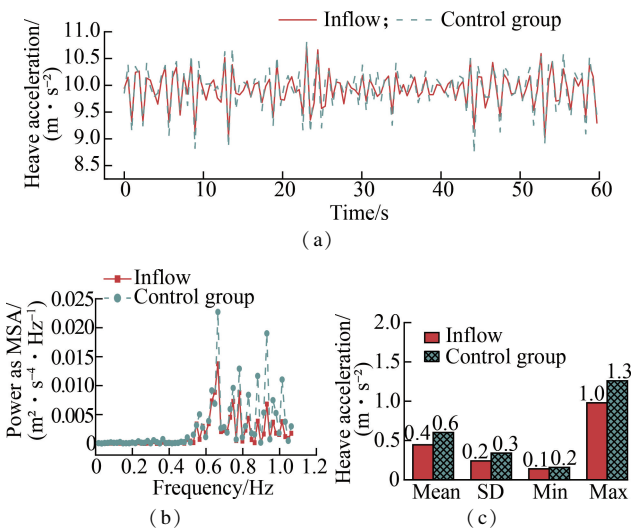

Fig. 14 Analysis of heave acceleration. (a) Time-history curve; (b) Power spectral density; (c) Mathematical statistics

Fig. 15 shows that the model not only undergoes short-term surge responses in the time domain with the wave frequency but also experiences a large-amplitude, long-period surge motion that deviates significantly from the equilibrium position. The surge power spectral density is mainly concentrated at approximately 0.067 Hz, corresponding to the inherent surge period of 15 s in the structure. A small amount of power is also concentrated at approximately 0.67 Hz, corresponding to the 1.5-s wave period. Mathematical statistical analysis indicates that the surge parameters in the inflow condition group are significantly smaller than those in the control group, with the maximum peak values exhibiting a decrease of 28%. The observed patterns under irregular wave conditions are consistent with those under regular waves discussed previously.

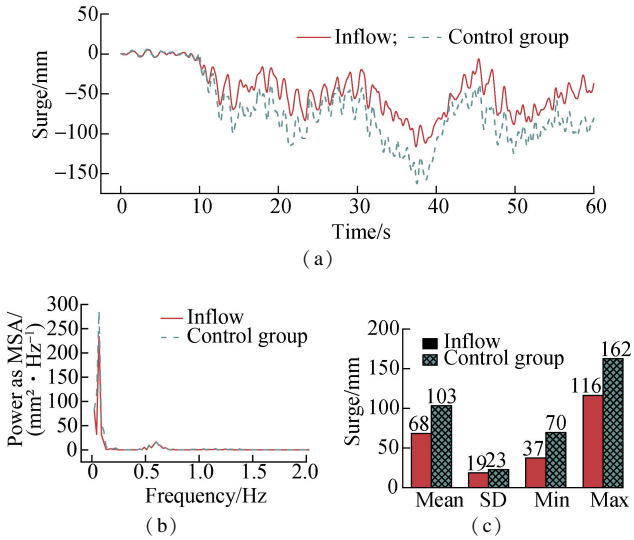

Fig. 15 Analysis of surge motion. (a) Time-history curve; (b) Power spectral density; (c) Mathematical statistics

As shown in Fig. 16, when the model is in equilibrium at the rest position, the initial static mooring force borne by the anchor chain is 7.9 N. The mooring force in the model not only responds briefly to the wave frequency but also exhibits large-amplitude, long-period responses. This finding is consistent with the conclusions drawn from the surge motion discussed previously. The power spectral density of the mooring force is mainly concentrated at approximately 0.067 Hz, corresponding to the inherent surge period of 15 s in the structure. After subtracting the initial mooring force from both sets of data obtained via mathematical statistical analysis, various parameters of the mooring force in the inflow condition group are significantly larger than those in the control group. The numerical relationship of the maximum peak value has increased by 39%. This phenomenon is attributed to the increase in the total mass of the model, which consequently

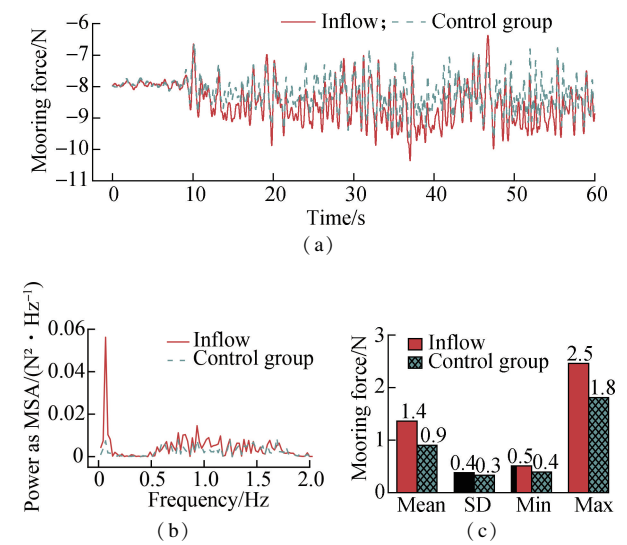

Fig. 16 Analysis of mooring force. (a) Time-history curve; (b) Power spectral density; (c) Mathematical statistics

renders the structure more challenging to constrain. In addition, this substantial augmentation is most pronounced as a result of the superposition of motions occurring in various directions. The observed phenomena under irregular wave conditions are consistent with the patterns observed under regular wave conditions, further validating the conclusions obtained.

4 Conclusions

1) The free decay tests show that the inherent periods of the structure for heave, surge, and pitch are approximately 1, 15, and 0.8 s, respectively, with minimal inflow impact.

2) Under hydrodynamic forces, the inflow condition and control groups exhibit similar motion patterns. However, the inflow condition group shows reduced heave, surge, and pitch acceleration, indicating smaller motion amplitudes than the control group.

3) Irregular waves cause both short-term surge responses and significant long-period deviations from equilibrium, affecting mooring force predictability. Under irregular wave conditions, the inflow has a significant impact on mooring force and structural motion.

4) The influence of inflow on mooring force and each motion of the structure is more significant under irregular wave conditions than under regular wave conditions.

References

[1] Cai S, Han D Q, Cha J R. Empirical research on vertical greening and energy saving technology in the range of architectural boundaries[J]. *Journal of Southeast University (English Edition)*, 2023, **39**(1): 33 - 48. DOI: 10.3969/j. issn. 1003-7985. 2023. 01. 005.

[2] Zhang P Y, Xiong L C, Le C H, et al. Comparison analysis of the bearing capacity of rock-socketed piles and sand piles for offshore wind turbines [J]. *Journal of Southeast University (English Edition)*, 2023, **39**(4): 384 - 392. DOI: 10. 3969/j. issn. 1003-7985. 2023. 04. 007.

[3] Ghosh A. A comprehensive review of water based PV: Flotavoltaics, under water, offshore & canal top [J]. *Ocean Engineering*, 2023, **281**: 115044. DOI: 10.1016/j. oceaneng. 2023. 115044.

[4] Essak L, Ghosh A. Floating photovoltaics: A review [J]. *Clean Technologies*, 2022, **4**(3): 752 - 769. DOI: 10. 3390/cleantechnol4030046.

[5] Sahu A, Yadav N, Sudhakar K. Floating photovoltaic power plant: A review[J]. *Renewable and Sustainable Energy Reviews*, 2016, **66**: 815 - 824. DOI: 10. 1016/j. rser. 2016. 08. 051.

[6] Khatib T, Mohamed A, Sopian K. A review of solar energy modeling techniques[J]. *Renewable and Sustainable Energy Reviews*, 2012, **16**(5): 2864 - 2869. DOI: 10. 1016/j. rser. 2012. 01. 064.

[7] Chen L. Singapore unveils one of the world's biggest floating solar panel farms [EB/OL]. (2021-07-14) [2023-12-11]. https://www. reuters. com/business/energy/singapore-unveils-one-worlds-biggest-floating-solar-panel-farms-2021-07-14/.

[8] Emiliano B. South Korea's largest floating PV plant now online[EB/OL]. (2021-11-25) [2023-12-21]. https://www. pv-magazine. com/2021/11/25/south-koreas-largest-floating-pv-plant-now-online-2/.

[9] Amir G. China commissions 320MW floating solar power plant[EB/OL] (2023-03-09) [2023-10-11]. https://www. offshore-energy. biz/china-commissions-320mw-floating-solar-power-plant/.

[10] KYOCERA. KYOCERA TCL Solar begins operation of Japan's largest 13.7MW floating solar power plant; Completion ceremony for plant on Yamakura Dam reservoir attended by governor of Chiba Prefecture | News Releases | KYOCERA[EB/OL]. (2023-04-10) [2023-11-10]. https://global. kyocera. com/news-archive/2018/0301_wvfh. html.

[11] White Pine Renewables. White pine renewables completes largest floating solar farm in the U. S. —White pine [EB/OL]. (2021-03-03) [2023-10-15]. https://whitepinerenewables. com/white-pine-renewables-completes-largest-floating-solar-farm-in-the-u-s/.

[12] Zimmerman. References-Zimmerman PV-floating [EB/OL]. (2023-04-18) [2023-11-17]. https://pv-floating. com/references/.

[13] Sanchez Molina P. Storage-linked 5 MW floating PV plant goes online in Portugal [EB/OL]. (2022-05-16) [2023-11-10]. https://www. pv-magazine. com/2022/05/16/storage-linked-5-mw-floating-pv-plant-goes-online-in-portugal/.

[14] Santos B. SPIC, Ocean Sun switch on offshore floating solar-wind pilot [EB/OL]. (2022-11-02) [2023-10-12]. https://www. pv-magazine. com/2022/11/02/spic-ocean-sun-build-worlds-first-offshore-floating-solar-wind-park/.

[15] Wang J, Lund P D. Review of recent offshore photovoltaics development[J]. *Energies*, 2022, **15**(20): 7462. DOI: 10. 3390/en15207462.

[16] Kjeldstad T, Lindholm D, Marstein E, et al. Cooling of floating photovoltaics and the importance of water temperature[J]. *Solar Energy*, 2021, **218**: 544 - 551. DOI: 10. 1016/j. solener. 2021. 03. 022.

[17] Ocean Sun. Banja | Ocean Sun[EB/OL]. (2023-12-05) [2023-12-30]. https://oceansun. no/project/banja/.

[18] Zhang P Y, Ding H Y, Le C H, et al. Towing characteristics of large-scale composite bucket foundation for offshore wind turbines[J]. *Journal of Southeast University (English Edition)*, 2013, **29**(3): 300 - 304. DOI: 10. 3969/j. issn. 1003-7985. 2013. 03. 013.

进水条件对浮式光伏膜结构水动力特性的影响

张浦阳　张林洋　熊粒超　乐丛欢　丁红岩

（天津大学水利工程智能建设与运维全国重点实验室，天津 300072）

摘要：选择 Ocean Sun 公司开发的浮动光伏膜结构原型作为参考对象，设计并制作了 1∶40 比例的实验室模型，旨在深入探讨流入条件对膜结构的水动力学特性的影响. 自由衰减测试结果显示，流入量对膜结构的垂荡、纵摇和纵荡的固有频率几乎没有影响. 这表明在不同的流入条件下，膜结构的动态特性基本保持稳定. 进一步进行的规则波和不规则波水动力实验结果表明，相较于对照组，流入条件下的膜结构在垂荡、纵摇、纵荡以及垂荡加速度运动方面的响应较为平缓，但系泊力较大. 特别是当波浪为不规则波时，流入条件对膜结构的影响更加显著，可能导致结构的响应变化更加复杂. 因此，在实际的工程设计过程中，必须充分考虑流入条件对膜结构行为的影响，并采取适当的工程措施来确保结构的安全性和稳定性.

关键词：浮式光伏；膜结构；水动力特性；入流条件

中图分类号：TM615